nature nanotechnology

SUPPLEMENTARY INFORMATION

https://doi.org/10.1038/s41565-017-0020-z

In the format provided by the authors and unedited.

# Peltier cooling in molecular junctions

**Longji Cui[1], Ruijiao Miao[1], Kun Wang[1], Dakotah Thompson[1], Linda Angela Zotti[2], Juan Carlos Cuevas[2,3]*, Edgar Meyhofer[1]* and Pramod Reddy[1,4]***

[1]Department of Mechanical Engineering, University of Michigan, Ann Arbor, MI, USA. [2]Departamento de Física Teórica de la Materia Condensada and Condensed Matter Physics Center (IFIMAC), Universidad Autónoma de Madrid, Madrid, Spain. [3]Department of Physics, University of Konstanz, Konstanz, Germany. [4]Department of Materials Science and Engineering, University of Michigan, Ann Arbor, MI, USA. *e-mail: juancarlos.cuevas@uam.es; meyhofer@umich.edu; pramodr@umich.edu

Supplementary Information for:

# Peltier Cooling in Molecular Junctions

*Longji Cui, Ruijiao Miao, Kun Wang, Dakotah Thompson, Linda Angela Zotti, Juan Carlos Cuevas, Edgar Meyhofer, Pramod Reddy*

**Supporting Information Contents:**

## 1. Nanofabrication process of suspended calorimetric devices

The detailed steps for fabricating the suspended calorimetric microdevices are shown in Fig. S1. Briefly, a low-stress silicon nitride ($SiN_x$) film that is 500 nm thick is first deposited onto a silicon wafer using LPCVD (Step 1). Subsequently, a 30 nm thick Pt serpentine line is patterned onto the $SiN_x$ layer using lift-off (Step 2). Then, Au leads with a thickness of 100 nm are defined on the $SiN_x$ layer using the same lift-off process (Step 3). The topology of the suspended region and the beams is created using RIE etching through the $SiN_x$ layer on the front side (Step 4). Windows in the $SiN_x$ layer, located on the backside of the silicon wafer, are then etched using RIE (Step 5). Subsequently, a through-hole in the silicon handler wafer is created by a KOH etch to release the suspended device (Step 6). After releasing the device, a 100 nm thick $Al_2O_3$ film is deposited on the whole device using atomic layer deposition (ALD) (Step 7) and serves to electrically isolate the Pt serpentine from the Au layer that will be deposited in the final step. Finally, the microdevice is coated with a 50 nm thick Au film that is deposited using sputtering (Step 8). Immediately after the deposition of the Au thin film, the microdevice is immersed into a molecular solution to form a self-assembled monolayer (SAM) of molecules.

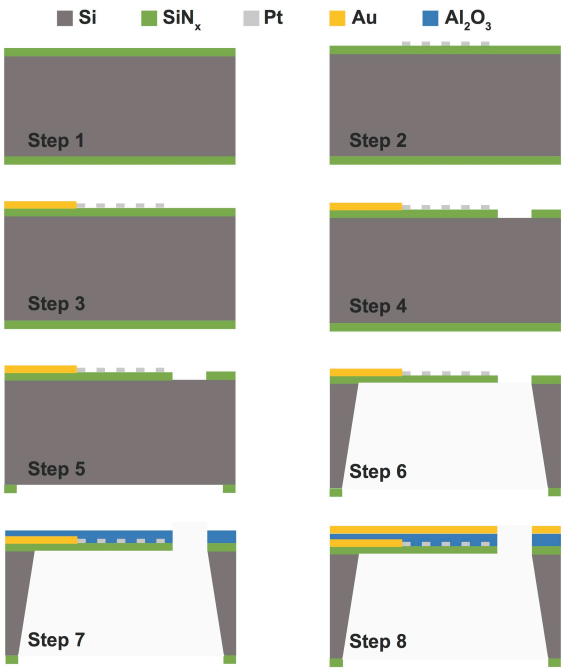


***Figure S1. Nanofabrication of the suspended calorimetric devices.*** *Detailed steps in the fabrication of the suspended calorimetric devices are described in the text.*

## 2. Measurement of the thermal resistance and thermal time constant of the calorimetric devices

The thermal resistance of the suspended microdevices was calibrated using an approach similar to that described in our previous work[1]. Briefly, the temperature rise of the device was measured by supplying a range of dc electrical currents to the integrated Pt serpentine line, which dissipated known amounts of heat in the suspended region of the microdevice. Figure S2a plots the measured temperature rise ($\Delta T$) against the power input ($Q$). The thermal resistance of the microdevice can be readily obtained by using $R_S = \Delta T / Q$, which was estimated to be 3.35 ($\pm$0.01) $\times 10^6$ K/W.

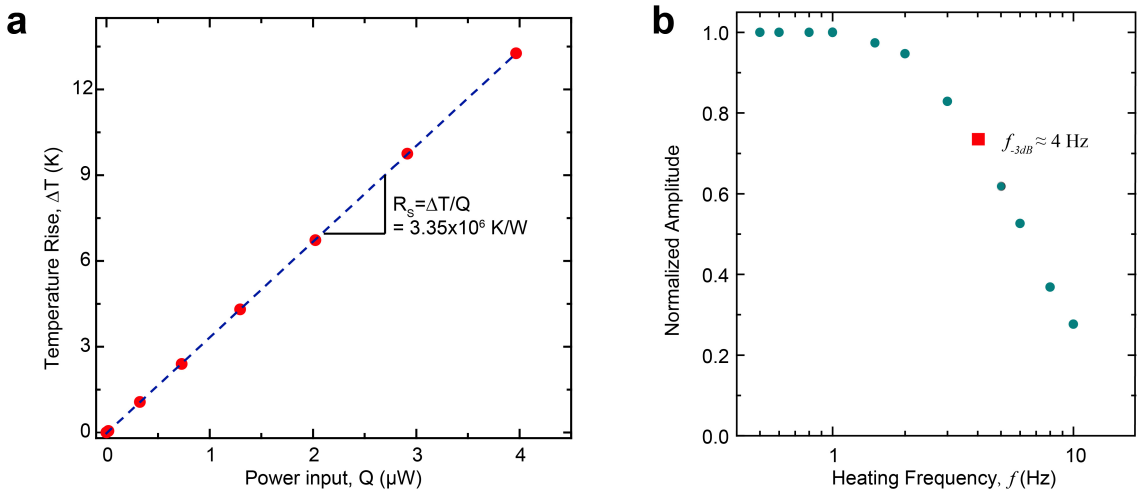


***Figure S2. Calibration of the thermal resistance and thermal time constant of the calorimetric devices. a,*** *Measured temperature rise of the device as a function of the input power. The thermal resistance is given by the slope of the fitted curve.* ***b,*** *Normalized temperature rise of the device as the frequency of the sinusoidal heat input is varied. The red square indicates the -3dB point.*

To calibrate the thermal time constant of the microdevice, we supplied a sinusoidal heat current with fixed amplitude ($I_f$ = 4 μA) and systematically varied the frequency of the current while measuring its temperature response. The Joule heating ($Q_{2f}$) occurs at a frequency $2f$ and produces temperature oscillations in the microdevice with an amplitude of $\Delta T_{2f}$. This $2f$ component of the temperature change of the microdevice can be related to the voltage drop across the Pt thermometer at $3f$, $V_{3f}$, using the relationship $V_{3f} = \Delta T_{2f} \alpha I_f R / 2$, where α is the

temperature coefficient of resistance and $R$ is the nominal resistance of the Pt thermometer. The measured amplitude of the temperature fluctuations, normalized to the amplitude of the measured value at the lowest frequency, is plotted against the frequency in Fig. S2b. We note that the cut-off frequency (-3dB point) is at ~4 Hz. Therefore, the thermal time constant ($\tau$) of the microdevice can be obtained using $\tau = (2\pi f_{-3\mathrm{dB}})^{-1} \sim 40$ ms.

### 3. Surface characterization of the microdevices

The surface topography of the Au-coated microdevices was characterized by atomic force microscopy (AFM). As shown in Fig. S3, the RMS roughness of the suspended region was found to be less than 0.4 nm within a scanning area of 500 nm by 500 nm. We note that this flatness is comparable to that for template-stripped Au surfaces and facilitates the formation of self-assembled monolayer of molecules on the Au surface.

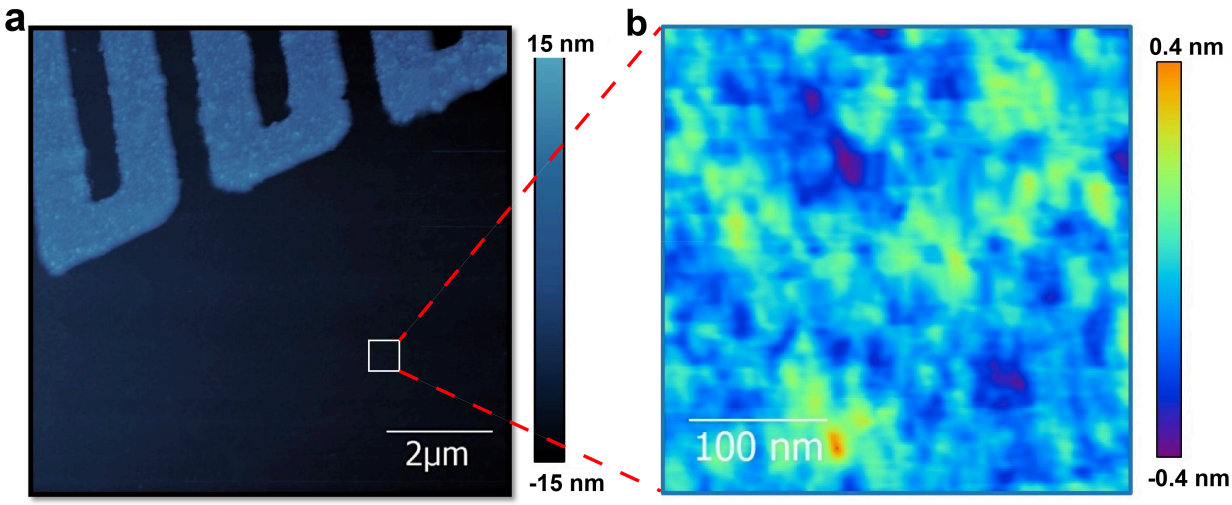


***Figure S3. Surface topography of the suspended microdevices obtained by Atomic Force Microscopy (AFM).*** *The Pt serpentine thermometer can be seen in (a).* ***b,*** *AFM scans performed on the planar region of the microdevice reveal a RMS roughness of ~0.4 nm within a 500 nm by 500 nm area.*

### 4. Calibration of the spring constant of the AFM probes

The spring constant of the AFM probes is estimated using the equipartition theorem[2]. Briefly, the spring constant of the AFM probe ($k$) and the temperature ($T$) of the thermal reservoir that the

probe is connected to are related by: $\frac{1}{2}k\langle x^2\rangle = \frac{1}{2}k_BT$ , where $k_B$ is the Boltzmann constant and $x$ is the displacement of the end of the tip due to random thermal fluctuation in the probe. To obtain the mean square displacement, $\langle x^2 \rangle$, we monitored the thermally-driven deflections of the AFM cantilever with a position-sensitive photodiode detector. From a time series of the AFM cantilever displacement we computed the power spectral density (PSD) of the thermally driven oscillations. As shown in Fig. S4, the PSD features a peak at ~13 kHz that corresponds to the resonant frequency of the AFM cantilever. The mean square displacement $\langle x^2 \rangle$ was obtained by integrating the PSD and was found to be ~0.039 nm$^2$. Finally, by substituting the estimated value of $\langle x^2 \rangle$ into the equipartition theorem the spring constant can be calculated to be ~0.1 N/m.

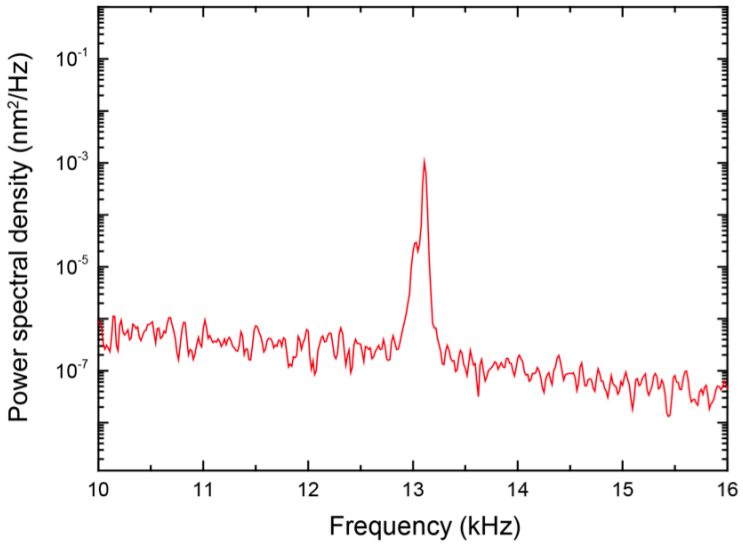


***Figure S4. Power spectral density (PSD) of the deflection of AFM cantilever.*** *The peak frequency at ~13 kHz corresponds to the resonance frequency of the cantilever, and the thermally-driven, mean squared displacement of the cantilever is about 0.039 nm$^2$.*

**5. Evaluation of the stiffness of the suspended calorimetric devices**

Thermal fluctuations of suspended microdevices need to be minimized to sub-nanometer levels for creating stable molecular junctions, which requires that the suspended devices have sufficiently high mechanical stiffness. To measure the stiffness of the calorimetric devices we employed an approach similar to that used in a previous work[3]. Briefly, we employed an AFM cantilever with a known spring constant ($k_{Can}$) of ~0.75 N/m and placed it in close proximity to a

solid silicon (Si) substrate. The substrate was first displaced towards the cantilever and the force exerted on the cantilever as a function of the displacement was recorded (Fig. S5). Subsequently, we systematically repeated the same experiments with a suspended device (suspended region attached to a Si substrate via thin and long beams, see Fig. 1). The measured force vs. displacement curves are shown in Fig. S5. It can be seen that the slope of the force vs. displacement curve ($m_1$) recorded on the solid substrate is greater than the curve ($m_2$) obtained with the compliant device. The difference in force exerted on the cantilever in the two experiments is attributable to the compliance of the suspended device. Specifically, it can be shown that the stiffness of the suspended device ($k_{Sus}$) can be related to the stiffness of the cantilever ($k_{Can}$) by the following expression $k_{Sus} = k_{Can} / \left[ (\frac{m_1}{m_2}) - 1 \right]$, which yields a stiffness for the microdevice of 3.85 ± 0.11 N/m. This stiffness is significantly higher than the stiffness of the AFM probes used in the measurement (~0.1 N/m) and thus does not limit the stability of our junctions.

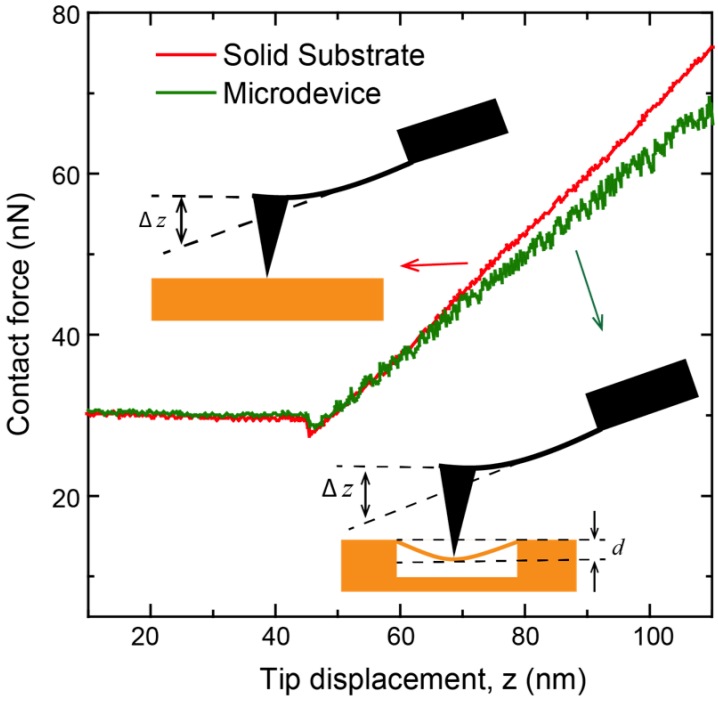


***Figure S5. Stiffness calibration of the suspended calorimeter. Force-displacement curves of an AFM probe on the calorimeter and a solid substrate.*** *The insets show the differences in deflection in the two different experiments. The stiffness of the microdevice calorimeter can be estimated from these measurements as described in the text.*

## 6. Analysis of the uniformity of the temperature distribution of the suspended calorimeters

In measuring the heating and cooling power of the molecular junctions, one important question is whether the temperature of the suspended region is uniform when heating or cooling occurs in a localized area. To address this issue, we employed a COMSOL-based finite element analysis to analyze the temperature distribution within the microdevice in the presence of a finite heat flux (300 nW) applied to a small spot (~20 $nm^2$) on the surface. Figure S6 presents the meshing topology used in the simulation and the calculated result. It can be clearly seen that the temperature drop occurs primarily along the beams connecting the suspended region to the thermal reservoir and there are negligible thermal gradients across the suspended region. This ensures that the temperature reported by the Pt thermometer integrated on the suspended region can be readily used to estimate the thermal power applied on the microdevice.

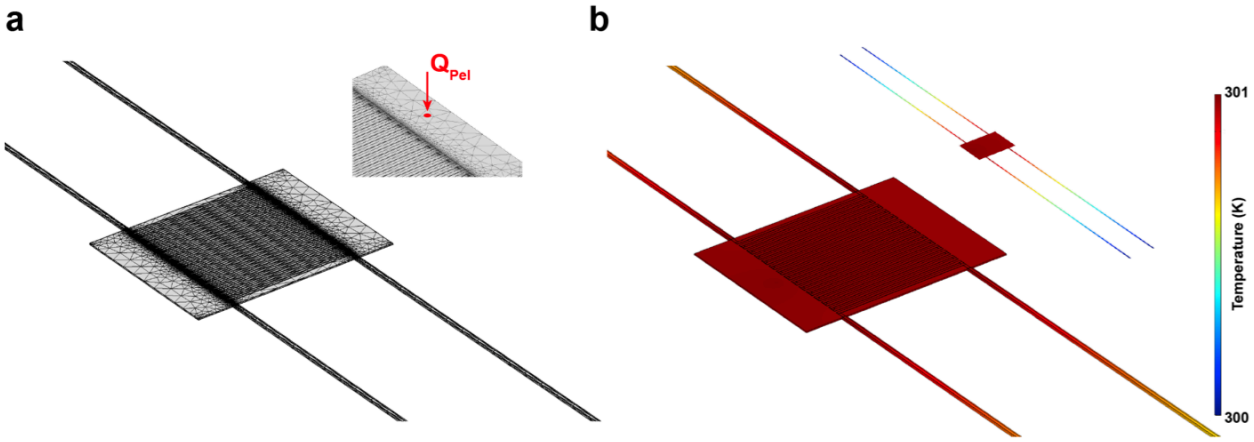


***Figure S6. Modelling of the temperature distribution on the calorimetric microdevice. a,*** *Meshing structure used in the simulation. A known amount of thermal power (300 nW) is applied to a small spot with an area of ~20 $nm^2$ at the edge of the suspended calorimeter device (see inset).* ***b****, Calculated temperature field when the temperature increases by ~1 K on the suspended region. The temperature gradient is primarily restricted to the beams (see inset).*

## 7. Ultra-low noise measurement environment

All measurements described in this work were performed using a ultra-high vacuum scanning probe microscope (RHK UHV 7500), which was housed in an ultra-low-noise facility that

features excellent vibration-isolation (meeting the stringent NIST-A criterion) and temperature stability (<100 mK drift over 24 hours).

**8. Characterization of the self-assembled monolayer of molecules**

We employed X-ray photoelectron spectroscopy (XPS) and ellipsometry to determine the monolayer thickness of the self-assembled monolayer. The representative measured results are presented in Fig. S7 and the estimated thicknesses are summarized in Table S1. The XPS experiments were performed on a Kratos Axis Ultra system using a monochromatic Al X-ray source at a setting of 8 mA and 14 kV. The estimated thickness is based on the exponential attention of the substrate photoelectrons in the presence of the self-assembled monolayer[4-7] (as shown in Fig. S7).

The ellipsometry measurements were performed on the Woollam M-2000 Ellipsometer. Incident light beams at angles of 55, 65 and 75 degree, over the wavelengths from 400-1700 nm were used for this characterization and the data were fit with an optical model (using CompleteEASE$^{TM}$ V4.86) to extract the thickness of the monolayer. It can be seen in Table S1 that the two measurement approaches yield consistent results, which agree well with previously reported thicknesses[8-11].

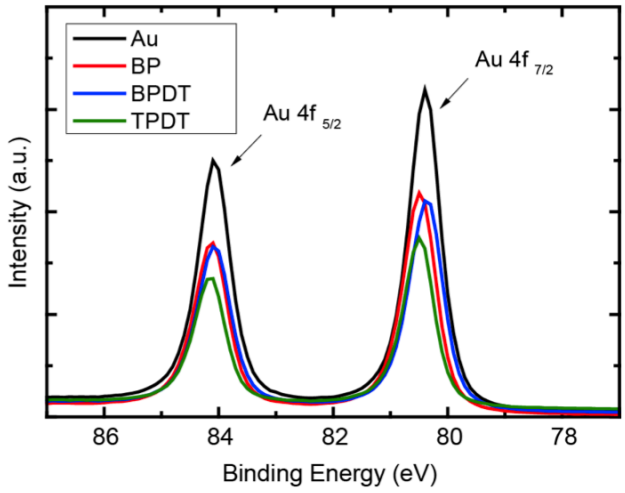


***Figure S7. Characterization of the self-assembled monolayer using XPS.*** *The photoelectron intensity on different monolayers as a function of the binding energy.*

***Table S1. Summary of the measured monolayer thicknesses using XPS and ellipsometry.***

| | BPDT | TPDT | BP |
|---|---|---|---|
| XPS (nm) | 1.29 (0.14) | 1.85 (0.19) | 1.19 (0.16) |
| Ellipsometry (nm) | 1.47 (0.07) | 1.86 (0.08) | 0.91 (0.08) |

The number of molecules in the junctions can be estimated by applying a simple, contact-mechanics model (Hertzian theory). Specifically, the radius of contact between the Au AFM tip and the SAM can be estimated from Hertzian contact mechanics[12] to be $r = \sqrt[3]{R_{tip}F/E}$, where $R_{tip}$ is the radius of the tip, $F$ is the apparent load on the contact, and $E$ is the Young's modulus. Taking $F$ to be 16 nN which sums the pull-off load of ~15 nN and the applied load of 1 nN, $R_{tip}$ = 100 nm, and $E$ = 79 GPa for Au, we estimate the contact radius $r$ to be 2.7 nm, corresponding to a contact area of ~23 nm$^2$. Based on the expected packing density of the benzene dithiol molecules on the Au[13] substrate of $\sim 5\times10^{14}$ molecules/cm$^2$ we estimate that the junction contains approximately 100-110 molecules. Moreover, we also employed the well-known Johnson-Kendall-Roberts (JKR) model[14] which was developed based on the classic Hertzian contact mechanics to calculate the contact area and didn't find significant difference in estimating the number of molecules compare to the classic model. Furthermore, the number of molecules in the junction can also be justified from the electrical conductance measurement. By comparing the reported value of the single-molecule junction, BPDT for example which is ~2.6 MΩ ($5\times10^{-3}G_0$)[15] to the measured electrical conductance of the SAM which is ~37 μS (27 KΩ), we can estimate the number of the molecules in the junction to be approximately 100, by assuming the electrical conduction of the molecules are independent from each other.

**9. Electric circuitry**

As depicted in Fig. 1a (main text), the low-bias electrical conductance of the molecular junctions is measured by applying a small voltage bias (below 20 mV) across the junctions and measuring the electric current using a current amplifier (Keithley 428). The current-flow in the molecular junctions generates both Peltier and Joule effects in the electrodes. The thermal power (heating or cooling) was measured by monitoring the temperature change of the suspended calorimeter

using the integrated Pt thermometer. This was accomplished by measuring the electrical resistance change of the Pt resistor in a half-Wheatstone bridge configuration whose voltage output was first amplified by an instrumentation amplifier (AD 524) with a gain of 100, and then supplied into a second voltage amplifier (SRS 760) with a gain of 10. Furthermore, current-voltage (I-V) characteristics of the molecular junctions were measured by linearly increasing the voltage bias (from ~ -0.5 V to 0.5 V) and measuring the resultant electric current. The approach employed for measuring the Seebeck coefficients of molecular junctions is shown in Fig. S8.

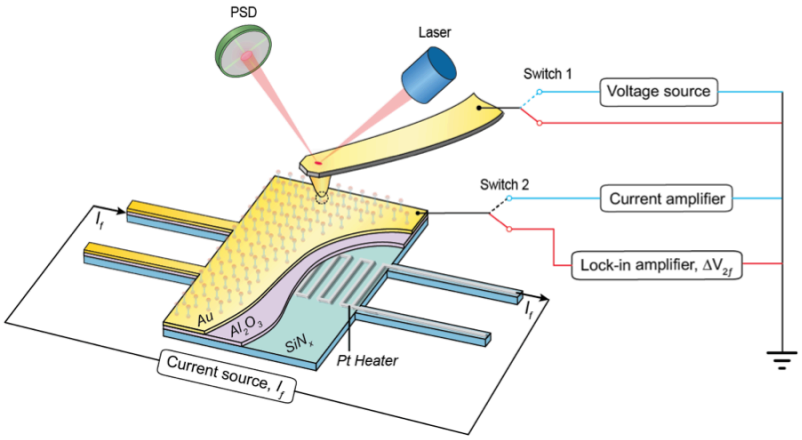


***Figure S8. Schematic describing the approach employed for thermoelectric voltage measurements on molecular junctions.***

Temperature change ( $\Delta T$ ) of the microdevice due to the Peltier cooling/Joule heating in the molecular junction can be estimated by $\Delta T = V_{Cal} / I_{in} R_{Pt} \alpha$ , where $V_{Cal}$ is the voltage output across the Pt thermometer, $I_{in}$ is the input electric current (see Fig. 1a) and $R_{Pt}$ and $\alpha$ are the resistance the temperature coefficient of resistance of the Pt thermometer, respectively. We note that the Joule heating induced by $I_{in}$ is estimated to elevate the temperature of the microdevice by ~10 K.

**10. Details of applying the time averaging scheme in data processing**

To implement the time averaging scheme measurements of heating and cooling in MJs, we applied repeated sequences of three level voltage biases across junctions and recorded the resulting electrical conductance and the temperature rise of the suspended calorimeter (as shown in Fig. 2a in the main text) for an extended period of time. Depending on the desired signal to

noise ratio and the magnitude of the thermal power output, the number of three-level periods over which data were collected was varied. Specifically, for the data shown in Fig. 2b the number of periods over which data were averaged at each bias are as follows: 450 (9 mV), 720 (8 mV), 1320 (7 mV), 600 (5 mV), 1500 (2 mV), and 2000 (1 mV), respectively. In general, the number of periods required to resolve signals increased with decreasing power output.

In performing these heat dissipation/cooling measurements we observed small changes in the electrical conductance of the junction (~5 % - 10 %) during the time course of the measurement. In order to (systematically) account for the variations of the conductance we normalized all the measured power outputs by the electrical conductance relative to that measured at a bias of 3 mV. Finally, we note that these results are independent of the samples and were found to be repeatable with multiple probes and microdevices calorimeters. An additional data set from a different microdevice and probe obtained over a wider range of biases for BPDT MJs is shown in Fig. S9. It can be seen the observed cooling minima is virtually identical to the data shown in Fig. 2c.

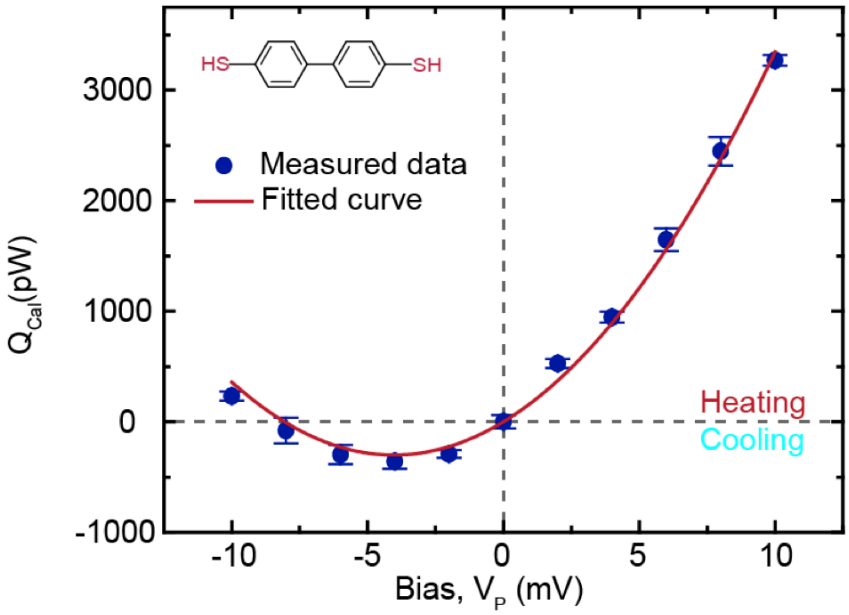


***Figure S9. Second independent data set for the voltage-dependent cooling/heat generation in BPDT junctions.*** *The solid red line indicates the fitted curve using Eq. 1 and the measured Seebeck coefficient and electrical conductance.*

## 11. Description of the temperature resolution of the Pt thermometer

To evaluate the temperature resolution of the Pt thermometer of the calorimeter, we followed the protocols developed by us in previous work[12, 13]. Briefly, our measurement applied an un-modulated electrical current into the Pt line to quantify the modulated temperature change due to the applied three-level voltage bias. The noise components in this experiment include contributions from the electronic system (amplifiers), thermal Johnson noise, shot noise, and the temperature fluctuation from the ambient environment. Following the procedure described in detail elsewhere[16] by us we estimate that the temperature resolution of our modulations based approach to be given by:

$$\Delta T_{\mathrm{Res}} = \left[ \int_0^{\infty} G_N(f) \left[ \frac{Sin(2\pi fT)}{(2\pi fT)} \right]^2 \times \left[ \frac{6Sin(\pi f \Delta t)}{1+2Cos(2\pi f \Delta t)} \right]^2 df \right]^{1/2} \qquad \text{(Eq. S1)}$$

where $G_{\mathrm{N}}(f)$ is the power spectral density associated with temperature noise, $3\Delta t = 5$ seconds (i.e. the period of each three level cycle) and $2T$ is the total time over which each set of three level excitations were performed. For example, as described in the section above for the bias with 1 mV amplitude, the three level excitation for this measurement was repeat for a total of 2000 cycles, where each cycle was 5 seconds long. Therefore, 2T = 2000×5 = 10,000 seconds for the 1 mV voltage amplitude experiments. Further, we note that we have previously[17] analyzed the noise spectral characteristics of resistance thermometers and had estimated $G_{\mathrm{N}}(f)$. Using this information in conjunction with Eq. S1, we estimate, that for measurements performed for 2000 cycles, our temperature resolution is better than 0.1 mK, thus giving us a heat current resolution that is below 30 pW.

## 12. Physical mechanisms of cooling and heat dissipation in molecular junctions

To qualitatively understand the physical processes that result in cooling we consider the schematics shown in Fig. S10 a-c where the left electrode is grounded and represents the electrode integrated into the calorimeter and the right electrode is negatively biased and represents the probe. In these scenarios electrons are injected into the right electrode (probe) at

an energy of $\mu_{\text{Cal}} + e|V_{\text{P}}|$ and leave the left electrode (calorimeter) at an energy $\mu_{\text{Cal}}$. This implies that if *N* electrons flow through the junction there is a net heat dissipation that is given by $Ne|V_{\text{P}}|$.

To understand the origin of cooling it is essential to first note that flow of charge occurs in a range of energies, *i.e.* at all energies between the chemical potentials of the electrodes and in a small range of energies (~few $k_B T$) above the chemical potential of the probe and below the chemical potential of the calorimeter. As is described in more detail below, the electrons flowing between the chemical potentials of the electrodes cause heating in both electrodes. However, the electrons flowing above the chemical potential of the probe ($\mu_{\text{Cal}} + e|V_{\text{P}}|$) produce heating in the calorimeter and cooling in the probe. Further, electrons flowing below the chemical potential of the calorimeter ($\mu_{\text{Cal}}$) cause cooling in the calorimeter and heating in the probe. From this discussion it is obvious that, for the given bias conditions, if the number of electrons transmitted below $\mu_{\text{Cal}}$ dominate the charge transfer then it is possible to achieve net cooling in the calorimeter. Below, we first describe the heating and cooling characteristics of electrons transmitted at various energies.

**Heating due to electrons transmitted between chemical potentials:** Fig. S10a shows the scenario where an electron is transmitted at an energy *E* between the chemical potentials. In this case the electron must dissipate as heat some of its energy ($\mu_{\text{Cal}} + e|V_{\text{P}}| - E$) in the probe and the rest of energy of ($E - \mu_{\text{Cal}}$) in the calorimeter. Thus, charge transfer at energies between the chemical potentials results in heat generation in both the electrodes and the total heat generation per electron is $e|V_{\text{P}}|$.

**Heating/Cooling due to electrons transmitted above the chemical potential of the probe:** When electrons are transmitted at an energy $E > \mu_{\text{Cal}} + e|V_{\text{P}}|$ (see Fig. S10b) the electrons absorb energy $E - \mu_{\text{Cal}} - e|V_{\text{P}}|$ from the probe resulting in cooling in the probe and dissipate energy $E - \mu_{\text{Cal}}$ in the calorimeter. Notice that the net heat generation by the electron in the device $((E - \mu_{\text{Cal}}) - (E - \mu_{\text{Cal}} - e|V_{\text{P}}|) = e|V_{\text{P}}|)$ is still the same as that for electrons transmitted between the chemical potentials.

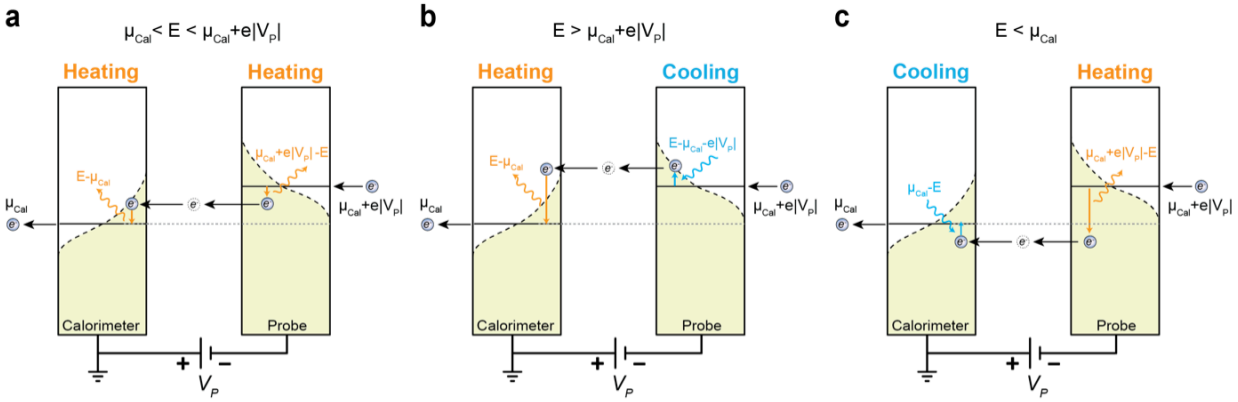


***Figure S10. Schematic describing the physical mechanism involved in heating and cooling in molecular junctions. a,*** *The scenario where an electron is transmitted between the chemical potentials of the electrodes.* ***b,*** *The scenario where an electron is transmitted above the chemical potential of the probe.* ***c,*** *The scenario where an electron is transmitted below the chemical potential of the calorimeter.*

**Heating/Cooling due to electrons transmitted below the chemical potential of the calorimeter:** When electrons are transmitted at an energy $E < \mu_{\mathrm{Cal}}$ (see Fig. S10c) they dissipate as heat some energy $(\mu_{\mathrm{Cal}} + e|V_{\mathrm{P}}| - E)$ in the probe resulting in heating of the probe and they absorb some energy $(E - \mu_{\mathrm{Cal}})$ in the calorimeter, resulting in cooling of the calorimeter. Again, notice that the net heat generation by the electron in the device $((E-\mu_{\mathrm{Cal}})-(E-\mu_{\mathrm{Cal}}-e|V_{\mathrm{P}}|)=e|V_{\mathrm{P}}|)$ is still the same as that for electrons transmitted between the chemical potentials.

**Relationship between transmission function and cooling:** From the qualitative description provided above it is clear that when the calorimeter electrode is grounded and the probe is negatively biased, net cooling can occur in the calorimeter if the cooling provided by electrons transmitted below $\mu_{\mathrm{Cal}}$ is larger than the heating produced by electrons transmitted at other energies. This can happen only when the transmission probabilities are larger at $\mu_{\mathrm{Cal}}$ than those at $\mu_{\mathrm{Cal}} + e|V_{\mathrm{P}}|$. This in turn implies that the transmission function has a negative slope, i.e. $(\partial T / \partial E)_{E=\mu_{Cal}}$ is negative, implying a positive Seebeck coefficient. This prediction is consistent with Eq. 1 of the manuscript, which suggests that when a negative bias is applied to the probe,

the calorimeter can be cooled if the Seebeck coefficient of the junction is positive. From the qualitative arguments provided above it can also be seen that, for net cooling to be observed, the heat dissipation due to electrons transmitted between the chemical potentials must also be small as they result in only heat dissipation. For this reason, cooling can only be observed at low voltage biases. Finally, if the transmission function is only weakly dependent on energy then the cooling due to electrons transmitted below $\mu_{\mathrm{Cal}}$ and heating due to electrons transmitted above $\mu_{\mathrm{Cal}} + e\left|V_{\mathrm{P}}\right|$ tend to cancel each other resulting in no observable cooling.

**Supplementary References:**


1. Cui, L. et al. Quantized thermal transport in single-atom junctions. *Science* **355**, 1192-1195 (2017).
2. Florin, E.L. et al. Sensing specific molecular-interactions with the atomic-force microscope. *Biosens. Bioelectron.* **10**, 895-901 (1995).
3. Frank, I.W., Tanenbaum, D.M., Van der Zande, A.M. & McEuen, P.L. Mechanical properties of suspended graphene sheets. *J. Vac. Sci. Technol. B* **25**, 2558-2561 (2007).
4. Henderson, J.I., Feng, S., Bein, T. & Kubiak, C.P. Adsorption of diisocyanides on gold. *Langmuir* **16**, 6183-6187 (2000).
5. Frey, S. et al. Structure of thioaromatic self-assembled monolayers on gold and silver. *Langmuir* **17**, 2408-2415 (2001).
6. Lu, Q. et al. From Tunneling to Hopping: A Comprehensive Investigation of Charge Transport Mechanism in Molecular Junctions Based on Oligo(p-phenylene ethynylene)s. *ACS Nano* **3**, 3861-3868 (2009).
7. Bain, C.D. & Whitesides, G.M. Attenuation lengths of photoelectrons in hydrocarbon films. *J. Phys. Chem.* **93**, 1670-1673 (1989).
8. Tan, A. et al. Effect of length and contact chemistry on the electronic structure and thermoelectric properties of molecular junctions. *J. Am. Chem. Soc.* **133**, 8838-8841 (2011).
9. Azzam, W., Wehner, B.I., Fischer, R.A., Terfort, A. & Woll, C. Bonding and orientation in self-assembled monolayers of oligophenyldithiols on Au substrates. *Langmuir* **18**, 7766-7769 (2002).
10. Kamenetska, M. et al. Conductance and Geometry of Pyridine-Linked Single-Molecule Junctions. *J. Am. Chem. Soc.* **132**, 6817-6821 (2010).
11. Diao, Y.X. et al. Adsorbed structures of 4,4 '-bipyridine on Cu(111) in acid studied by STM and IR. *Langmuir* **22**, 3640-3646 (2006).
12. Johnson, K.L. Contact mechanics. (Cambridge University Press; 1985).
13. Whelan, C.M., Smyth, M.R. & Barnes, C.J. HREELS, XPS, and electrochemical study of benzenethiol adsorption on Au(111). *Langmuir* **15**, 116-126 (1999).
14. Johnson, K.L., Kendall, K. & Roberts, A.D. Surface Energy and Contact of Elastic Solids. *Proc. R. Soc. Lon. A* **324**, 301-& (1971).
15. Guo, S.Y., Zhou, G. & Tao, N.J. Single Molecule Conductance, Thermopower, and Transition Voltage. *Nano Lett.* **13**, 4326-4332 (2013).
16. Lee, W. et al. Heat dissipation in atomic-scale junctions. *Nature* **498**, 209-212 (2013).
17. Sadat, S., Meyhofer, E. & Reddy, P. High resolution resistive thermometry for micro/nanoscale measurements. *Rev. Sci. Instrum.* **83** (2012).